
Confronting Ambiguity in 6D Object Pose Estimation via Score-Based Diffusion on $SE(3)$

Tsu-Ching Hsiao¹, Hao-Wei Chen¹, Hsuan-Kung Yang¹, Chun-Yi Lee¹

Abstract

Addressing accuracy limitations and pose ambiguity in 6D object pose estimation from single RGB images presents a significant challenge, particularly due to object symmetries or occlusions. In response, we introduce a novel score-based diffusion method applied to the $SE(3)$ group, marking the first application of diffusion models to $SE(3)$ within the image domain, specifically tailored for pose estimation tasks. Extensive evaluations demonstrate the method's efficacy in handling pose ambiguity, mitigating perspective-induced ambiguity, and showcasing the robustness of our surrogate Stein score formulation on $SE(3)$. This formulation not only improves the convergence of Langevin dynamics but also enhances computational efficiency. Thus, we pioneer a promising strategy for 6D object pose estimation.

1 Introduction

Estimating the six degrees of freedom (DoF) pose of objects from a single RGB image remains a formidable task, primarily due to the presence of ambiguity induced by symmetric objects and occlusions. Symmetric objects exhibit identical visual appearance from multiple viewpoints, which makes it difficult to differentiate among their various orientations. On the other hand, occlusions arise when part of an object is obstructed from view by another object or its own structure, which can obscure crucial details necessary to determine the complete shape and orientation of the object. Pose ambiguity presents a unique challenge as it transforms the direct one-to-one correspondence between an image and its associated object pose into a complex one-to-many scenario. As a result, a single observed image might correspond to several potential poses, which leads to significant performance degradation for methods reliant on one-to-one correspondence. Despite extensive exploration in the object pose estimation literature [1–5], pose ambiguity remains a persisting and unresolved issue.

In the face of these challenges, recent advancements in pose regression have introduced the use of symmetry-aware annotations to improve pose estimation accuracy [1, 6–8]. These methods typically employ symmetry-aware and surrogate losses that can tackle the pose ambiguity problem. The applicability and efficacy of these losses, nevertheless, depend on the provision of symmetry annotations that characterize the symmetrical properties of objects. Although the acquisition of these annotations for objects with distinct symmetry is relatively straightforward, it becomes a considerably complex task for objects with complex shapes or under occlusion. An example is a texture-less cup, where the true orientation becomes ambiguous if the handle is not visible. Furthermore, real-world applications usually present partially observed environments, where objects may appear in various orientations and with degrees of occlusion. The manual labor and time required to annotate the symmetry of each object under such circumstances is impractical. As a result, despite the potential of symmetry-aware annotations in addressing pose ambiguity, securing these annotations, particularly in complex and partially observed environments, presents an obstacle in object pose estimation.

Several contemporary studies have sought to circumvent the difficulties associated with obtaining symmetry annotations by reframing the original pose estimation problem as a density estimation problem. By treating ‘equivalent poses’ as a multi-modal distribution, methods such as Implicit-

¹Elsa Lab, Department of Computer Science, National Tsing Hua University, Hsinchu City, Taiwan

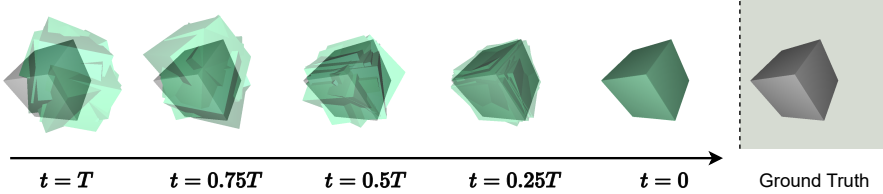


Figure 1: Visualization of the denoising process of our $SE(3)$ score-based model for 6DoF pose estimation.

PDF [4], HyperPose-PDF [9], and SpyroPose [10] leverage deep neural networks (DNNs) to implicitly characterize the non-parametric density on the rotation manifold $SO(3)$. This enables them to estimate poses without explicit reliance on symmetry annotations. While these advances are noteworthy, they also introduce new complexities. For instance, the computation of the maximum likelihood loss during training requires exhaustive sampling across the whole $SO(3)$ space. Moreover, the accuracy of inference is dependent on the resolution of the grid search, which necessitates a significant amount of grid sampling. These computationally demanding approaches may not only restrict the achievable precision of pose estimation, but also present obstacles when extending to larger spaces such as $SE(3)$ due to the substantial memory requirements. Despite the innovative strides made in utilizing implicit density representation for pose estimation, the computational intensity and resource demands associated with these methods present significant impediments for their practical applications.

Recognizing these challenges, the research community is pivoting towards diffusion models (DMS) [11–14]. These models have demonstrated promise in managing complex and multi-modal problems. Specifically, diffusion models are adept at efficiently tackling multi-modal distributions, an attribute that could be advantageous in addressing pose ambiguity issues. Their effectiveness lies in the iterative sampling process, which incorporates noise and enables a more focused exploration of the pose space while reducing computational demands. Moreover, diffusion models excel in terms of scalability, providing the capacity for managing larger spaces involving considerable parameters. This scalability is primarily due to the ability of these models to learn complex and high-dimensional distributions without the need for explicit density estimation. Given these attributes, diffusion models offer a promising solution to the computational intensity and resource demands for pose estimation tasks. In previous endeavors, the authors [15, 16] applied the denoising diffusion probabilistic model (DDPM) [12] and score-based generative model (SGM) [14] to the $SO(3)$ space, and achieved superior results in recovering unknown densities on the $SO(3)$ rotation manifold. Meanwhile, other research efforts [17, 18] have extended the application of diffusion models to the more complex $SE(3)$ space. Unfortunately, it is crucial to note that these studies concentrated on the vector space, without extending their techniques to the image space or specifically applying them to object poses.

In light of the above motivations, in this paper, we introduce a novel approach that applies diffusion models to the $SE(3)$ group for object pose estimation tasks, specifically aimed at addressing the pose ambiguity problem. This method draws its inspiration from the correlation observed between rotation and translation distributions, a phenomenon often resultant from the perspective effect inherent in image projection. We propose that by jointly estimating the distribution of rotation and translation on $SE(3)$, we may secure more accurate and reliable results as shown in Fig. 1. To the best of our knowledge, this is the first work to apply diffusion models to $SE(3)$ within the context of image space. To substantiate our approach, we have developed a new synthetic dataset, called SYMSOL-T, based on the original SYMSOL dataset [4]. SYMSOL-T enriches the original SYMSOL dataset by incorporating randomly sampled translations, thus providing a more rigorous testbed for evaluating the effectiveness of our method in capturing the joint density of object rotations and translations.

Following the motivations discussed, we have extensively evaluated our $SE(3)$ diffusion model using the synthetic SYMSOL-T dataset. The experimental results affirm the model’s competence in handling $SE(3)$, successfully addressing the pose ambiguity problem in 6D object pose estimation. Moreover, the diffusion model has proven effective in mitigating ambiguities introduced by image perspective effects. Importantly, the surrogate Stein score formulation we propose on $SE(3)$ exhibits improved convergence in Langevin dynamics compared to the score calculated via automatic differentiation. This not only underscores the robustness of our formulation, but also demonstrates its potential to handle complex dynamics in object pose estimation tasks.

2 Background

2.1 Lie Groups and Their Application in Pose Estimation

A Lie group represented as \mathcal{G} , serves as a cornerstone in the mathematical framework for pose estimation, due to the concepts of group and smooth (or differentiable) manifold, which is a topological space that locally resembles linear space. Importantly, following the group axioms, the composition operation is ensured to be denoted as $\circ : \mathcal{G} \times \mathcal{G} \rightarrow \mathcal{G}$, and the inversion map, both exhibit smoothness in relation to the group structure. For simplicity, we denote the composition operator between two group elements $X, Y \in \mathcal{G}$ as $X \circ Y = XY$ in the following content. Every Lie group \mathcal{G} has an associated Lie algebra, denoted as \mathfrak{g} . Lie group with its Lie algebra are related through the following mappings: $\text{Exp} : \mathfrak{g} \rightarrow \mathcal{G}$, $\text{Log} : \mathcal{G} \rightarrow \mathfrak{g}$. In the realm of pose estimation, there are two commonly used Lie groups: $SO(3)$ and $SE(3)$. The Lie group $SO(3)$, together with its associated Lie algebra $\mathfrak{so}(3)$, represents rotations in the Euclidean space. On the other hand, the Lie group $SE(3)$ and its corresponding Lie algebra $\mathfrak{se}(3)$ describe rigid-body transformations. Rigid-body transformations include both rotations and translations in Euclidean space. Such group structures construct the mathematical basis for analyzing and solving pose estimation problems, particularly dealing with six Degrees of Freedom (6DoF) pose estimation.

2.2 Parametrization of $SE(3)$

The special Euclidean group $SE(3)$ is a fundamental group for studying rigid-body motions as it encompasses both rotations and translations in three-dimensional Euclidean space. While various parametrizations for $SE(3)$ are presented in [19], in this work, we consider two parametrizations.

The first type of parametrization separates the rotations $R \in SO(3)$ and translations $T \in \mathbb{R}^3$ to form a composite manifold $\langle \mathbb{R}^3, SO(3) \rangle$ and its lie algebra $\langle \mathbb{R}^3, \mathfrak{so}(3) \rangle$, namely $R^3 SO(3)$. It has the composition rule defined as $(R_2, T_2)(R_1, T_1) = (R_2 R_1, T_2 + T_1)$. This parametrization is widely used in the previous diffusion models on $SE(3)$ considering its simplicity [18, 17], which induce a separated diffusion process for both R and T .

Another parametrization is the well-known $SE(3)$. We denote its element in Lie algebra as $\tau = (\rho, \phi) \in \mathfrak{se}(3)$ and its corresponding group element $(R, T) = (\text{Exp}(\phi), \mathbf{J}_l(\phi)\rho) \in SE(3)$, where \mathbf{J}_l is the left-Jacobian on $SO(3)$. The composition rule for $SE(3)$ parametrization is defined as $(R_2, T_2)(R_1, T_1) = (R_2 R_1, T_2 + R_2 T_1)$. This interconnection between rotations and translations in $SE(3)$ results in a diffusion process that mimicking the intricate dynamics of rigid-body motion, enhancing the fidelity of the diffusion model.

2.3 Score-Based Generative Modeling

The (*Stein*) score of a probability density $p(\mathbf{x})$ is defined as $\nabla_{\mathbf{x}} \log p(\mathbf{x})$. Consider an i.i.d samples $\{\mathbf{x}_i \in \mathbb{R}^D\}_{i=1}^N$ generated by a data distribution $p_{\text{data}}(\mathbf{x})$. In score-based generative models (SGMs), a primary formulation of diffusion models, data is incrementally transformed into a simple known prior distribution (e.g., Gaussian distribution) in the *forward* process. Consider a sequence of increasing positive noise scales $\{\sigma_i\}_{i=1}^L$, with $\sigma_{\min} = \sigma_1 < \sigma_2 < \dots < \sigma_L = \sigma_{\max}$. σ_{\min} and σ_{\max} are small and large enough to approximate $p_{\sigma_{\min}}(\mathbf{x})$ to $p_{\text{data}}(\mathbf{x})$, and $p_{\sigma_{\max}}(\mathbf{x})$ to $\mathcal{N}(\mathbf{x}; \mathbf{0}, \sigma_{\max}^2 \mathbf{I})$ respectively. The forward process is formulated with a perturbation kernel $p_{\sigma}(\tilde{\mathbf{x}}|\mathbf{x}) := \mathcal{N}(\tilde{\mathbf{x}}; \mathbf{x}, \sigma^2 \mathbf{I})$ and $p_{\sigma}(\tilde{\mathbf{x}}) := \int p_{\text{data}}(\mathbf{x}) p_{\sigma}(\tilde{\mathbf{x}}|\mathbf{x}) d\mathbf{x}$. In NCSN [11], a network $s_{\theta}(\mathbf{x}, \sigma)$ is trained using a Denoising Score Matching objective [20] as follow:

$$\theta^* = \arg \min_{\theta} \mathcal{L}(\theta; \sigma) \triangleq \frac{1}{2} \mathbb{E}_{p_{\text{data}}(\mathbf{x})} \mathbb{E}_{\tilde{\mathbf{x}} \sim \mathcal{N}(\mathbf{x}, \sigma^2 \mathbf{I})} \left[\|s_{\theta}(\tilde{\mathbf{x}}, \sigma) - \nabla_{\tilde{\mathbf{x}}} \log p_{\sigma}(\tilde{\mathbf{x}}|\mathbf{x})\|_2^2 \right] \quad (1)$$

Ideally, the optimal score-based model $s_{\theta^*}(\mathbf{x}, \sigma)$ matches $\nabla_{\mathbf{x}} \log p(\mathbf{x})$ almost everywhere for $\sigma \in \{\sigma_i\}_{i=1}^L$. As for generating samples, SGMs apply the iterative *reverse* process. In NCSN [11], they leverage the Langevin MCMC to run M steps to produce a sample for each $p_{\sigma_i}(\mathbf{x})$ sequentially:

$$\tilde{\mathbf{x}}_i^m = \tilde{\mathbf{x}}_i^{m-1} + \epsilon_i s_{\theta^*}(\tilde{\mathbf{x}}_i^{m-1}, \sigma_i) + \sqrt{2\epsilon_i} \mathbf{z}_i^m, \quad m = 1, 2, \dots, M, \quad (2)$$

where $\epsilon_i > 0$ is the step size, and \mathbf{z}_i^m is standard normal.

Overall, diffusion models, and particularly SGMs, provide a robust framework for handling complex data distributions, and they serve as the foundation for the denoising procedure of our methodology.

Baselines	Group	Distribution	Closed Form	Diffusion Method	Diffusion Space
Leach <i>et al.</i> [15]	$SO(3)$	$IG_{SO(3)}$	✗	DDPM	$SO(3)$
Jagvaral <i>et al.</i> [16]	$SO(3)$	$IG_{SO(3)}$	✗	Score / Autograd	$SO(3)$
Urain <i>et al.</i> [17]	$R^3SO(3)$	$\mathcal{N}_{\mathbb{R}^3} \times \mathcal{N}_{SO(3)}$	✓	Score / Autograd	$R^3SO(3)$
Yim <i>et al.</i> [18]	$R^3SO(3)$	$\mathcal{N}_{\mathbb{R}^3} \times IG_{SO(3)}$	✗	Score / Autograd	$(\mathbb{R}^3, \mathfrak{so}(3))$
Ours	$SE(3)$	$\mathcal{N}_{SE(3)}$	△	Score / Closed Form	$SE(3)$

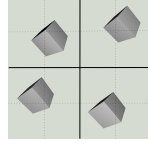


Figure 2: **Left:** Comparison of different methods. \triangle means closed form but with approximation. $\mathcal{N}_{SE(3)}$ please refer to Eq. (3). **Right:** Visualizing pose ambiguity caused by image perspective. The rotations between the four cubes differ by an angle of 15 degrees.

3 Preliminaries

3.1 Comparative Analysis of Diffusion Models in Pose Estimation

Diffusion models have been successfully employed for pose estimation tasks [15–18]. However, the selection of distribution and computation methods varies across different implementations, leading to differing outcomes and computational efficiencies. Fig. 2 provides a comparison of prior diffusion model approaches used in pose estimation along with ours. It highlights the distinctive groups, distributions, methods, as well as diffusion spaces each employs. Several earlier studies [15, 16] proposed approaches operating within the $SO(3)$ space and employs normal distributions on $SO(3)$ [21] (denoted as $IG_{SO(3)}$). A significant limitation of $IG_{SO(3)}$ is the lack of a closed form, which imposes computational constraints. Similarly, the method proposed by [18] operates in the tangent space of $SE(3)$ parameterized with $R^3SO(3)$ (represented as $r3so3$). Its distribution lacks a closed form as well, posing challenges to its computational efficiency. On the other hand, the authors in [17] employed a joint Gaussian distribution in the \mathbb{R}^3 and $SO(3)$ spaces, which does possess a closed form, potentially enhancing computational efficiency. Unfortunately, this method operates within the $R^3SO(3)$ space and might not fully exploit the benefits offered by the $SE(3)$ space.

3.2 The Benefits of $SE(3)$ over $R^3SO(3)$ in Perspective-Affected Pose Estimation

In the realm of pose estimation, the effect of image perspective present a notable challenge. It intertwines rotation and translation in the image space, leading to the phenomenon of pose ambiguity. Fig. 2 (right) exemplifies this through four cubes, each of which appears similarly oriented but actually differs in rotation degrees, complicating model predictions for accurate rotation angles. The parametrizations of R^3SO3 and $SE(3)$ offer different approaches to dealing with this problem. Specifically, R^3SO3 does not factor in the relationship between rotation and translation, whereas $SE(3)$ actively incorporates it into its structure. As a result, it is reasonable to hypothesize that $SE(3)$ might be more capable of mitigating performance degradation stemming from the image perspective effect. This potential advantage of $SE(3)$, further elaborated in Section 2.2, presents an intriguing avenue for future exploration in pose estimation research.

4 Methodology

4.1 Problem Formulation

To apply score-based generative modeling to a Lie group \mathcal{G} , we first establish a perturbation kernel on \mathcal{G} that conforms to the Gaussian distribution, as proposed by [22, 23]. The kernel is expressed as:

$$p_\Sigma(Y|X) := \mathcal{N}_{\mathcal{G}}(Y; X, \Sigma) \triangleq \frac{1}{\zeta(\Sigma)} \exp \left(-\frac{1}{2} \text{Log}(X^{-1}Y)^\top \Sigma^{-1} \text{Log}(X^{-1}Y) \right), \quad (3)$$

where Σ represents a covariance matrix filled with σ on the diagonal, $\zeta(\Sigma)$ denotes a normalizing constant, and $X, Y \in \mathcal{G}$ are group elements. The *score* on \mathcal{G} corresponds to the gradient of the log-density of the data distribution relative to the group element Y . It can be formulated as follows:

$$\nabla_Y \log p_\Sigma(Y|X) = -\mathbf{J}_r^{-\top} (\text{Log}(X^{-1}Y)) \Sigma^{-1} \text{Log}(X^{-1}Y). \quad (4)$$

This term can be expressed in a closed form if the inverse of the right-Jacobian \mathbf{J}_r^{-1} on \mathcal{G} also has a closed form. However, an alternative approach suggested by [17] would be to compute this term using automatic differentiation. By substituting Y with \tilde{X} , where $\tilde{X} = X\text{Exp}(z)$, $z \sim \mathcal{N}(0, \sigma_i^2 I)$,

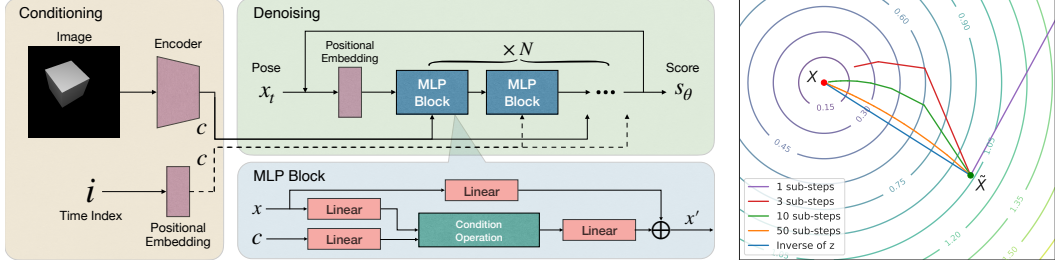


Figure 3: **Left:** An overview of the framework. **Right:** Visualization of a denoising step from a noisy sample \tilde{X} to its cleaned counterpart X on $SE(2)$. The contours illustrate the distances to X in 2D Euclidean space, while each line represents a denoising path with varying sub-sampling steps.

and integrating the above definition, the *score* on \mathcal{G} can be reformulated as follows:

$$\nabla_Y \log p_\sigma(\tilde{X}|X) = -\frac{1}{\sigma^2} \mathbf{J}_r^{-\top}(z) z. \quad (5)$$

A score model $s_\theta(\tilde{X}, \sigma)$, can then be trained using the Denoising Score Matching objective in Eq. (1):

$$\theta^* = \arg \min_{\theta} \mathcal{L}(\theta; \sigma) \triangleq \frac{1}{2} \mathbb{E}_{p_{\text{data}}(X)} \mathbb{E}_{\tilde{X} \sim \mathcal{N}_{\mathcal{G}}(X, \Sigma)} \left[\left\| s_\theta(\tilde{X}, \sigma) - \nabla_{\tilde{X}} \log p_\sigma(\tilde{X}|X) \right\|_2^2 \right] \quad (6)$$

To complete the process, we employ a variant of Langevin Dynamics [24], tailored to the Lie group context, as a means to generate a sample from a noise. The procedure can be expressed as follows:

$$\tilde{X}_{i+1} = \tilde{X}_i \text{Exp}(\epsilon_i s_\theta(\tilde{X}_i, \sigma_i) + \sqrt{2\epsilon_i} z_i), \quad z_i \sim \mathcal{N}(0, I). \quad (7)$$

4.2 Efficient Computation of Stein Score

In Section 4.1, we introduced the application of score-based generative modeling to a Lie group \mathcal{G} . The *score* can be computed via either automatic differentiation or a closed-form expression. However, obtaining the closed-form *score* presents a challenge due to its dependency on the distribution selection. For instance, deriving the closed-form *score* induced by $IG_{SO(3)}$ [21] can be challenging. Moreover, the computation of the *score* relies on the availability of a closed-form expression for the Jacobian matrix on \mathcal{G} . Even if such an expression is available, it may not necessarily offer computational savings compared to automatic differentiation. Therefore, we next discuss a simplification method of the Stein score under certain conditions for reducing computational costs on the Lie group.

The Stein score, induced by $\mathcal{N}_{\mathcal{G}}$, can be expressed in closed-form if the Jacobian matrix on \mathcal{G} is invertible and if the left and right Jacobian matrices conform to the relation described as follows:

$$\mathbf{J}_l(z) = \mathbf{J}_r^\top(z), \quad \mathbf{J}_l^{-1}(z) = \mathbf{J}_r^{-\top}(z), \quad (8)$$

where $z \in \mathfrak{g}$. As pointed out by [19], $SO(3)$ exhibits this property, and the closed-form *score* on $SO(3)$ can be simplified by demonstrating the following property, which holds on any \mathcal{G} :

$$\mathbf{J}_l(z)z = z. \quad (9)$$

The derivation is in the supplementary material. The *score* on $SO(3)$ can then be reformulated as:

$$\nabla_Y \log p_\sigma(\tilde{X}|X) = -\frac{1}{\sigma^2} \mathbf{J}_l^{-1}(z)z = -\frac{1}{\sigma^2} z. \quad (10)$$

This demonstrates that the *score* on $SO(3)$ can be simplified to the sampled Gaussian noise z scaled by $-1/\sigma^2$, thus eliminating the need for both automatic differentiation and Jacobian calculations. Similarly, the *score* on $R^3SO(3)$ has a closed-form as its Jacobians satisfy the relations of Eq. (8):

$$\mathbf{J}_l(z) = (I, \mathbf{J}_l(\phi)) = (I, \mathbf{J}_r^\top(\phi)) = \mathbf{J}_r^\top(z), \quad (11)$$

where $z = (T, \phi) \in \langle \mathbb{R}^3, \mathfrak{so}(3) \rangle$. This implies that the *score* on $R^3SO(3)$ can also be simplified to the formulation represented by Eq. (10).

4.3 Surrogate Stein Score Calculation on $SE(3)$

The preceding sections have explained how the selection of an appropriate Gaussian kernel enables the simplification of the *score* on $SO(3)$ and $R^3SO(3)$ to sampled Gaussian noise. While this insight may suggest the feasibility of a similar simplification of the *score* calculation on $SE(3)$, we demonstrate that $SE(3)$ does not conform to the property outlined in Eq. (8). The inverse of the left-Jacobian on $SE(3)$ at $z = (\rho, \phi) \in \mathfrak{se}(3)$ is given by $\mathbf{J}_l^{-1}(z) = \begin{bmatrix} \mathbf{J}_l^{-1}(\phi) & \mathbf{Z}(\rho, \phi) \\ 0 & \mathbf{J}_l^{-1}(\rho) \end{bmatrix}$ where $\mathbf{Z}(\rho, \phi) = -\mathbf{J}_l^{-1}(\phi)\mathbf{Q}(\rho, \phi)\mathbf{J}_l^{-1}(\phi)$. The full form of $\mathbf{Q}(\rho, \phi)$ can be found in [19, 25] and our supplementary material. By showing $\mathbf{Q}^\top(-\rho, -\theta) = \mathbf{Q}(\rho, \theta)$, we derive the following inequality:

$$\mathbf{J}_r^{-\top}(z) = (\mathbf{J}_l^{-1}(-z))^\top = \begin{bmatrix} \mathbf{J}_l^{-1}(\rho) & 0 \\ \mathbf{Z}(\rho, \phi) & \mathbf{J}_l^{-1}(\rho) \end{bmatrix} \neq \mathbf{J}_l^{-1}(z). \quad (12)$$

This inequality indicates the potential discrepancy between the *score* vector and the denoising direction due to the curvature of the manifold, which may impede the convergence of Langevin dynamics and necessitate additional denoising steps. To address this problem, we turn to higher-order approximation methods by breaking one Langevin dynamics step into multiple smaller sub-steps. Fig. 3 (right) illustrates this one-step denoising process on $SE(2)$ from a noisy sample $\tilde{X} = X\text{Exp}(z)$ to its cleaned counterpart X , with contour lines representing the distance to X in 2D Euclidean space. We observe that increasing the number of sub-steps eventually leads the integral of those *small* transformations approaches the inverse transformation of z . As a result, we propose substituting the *true score* in Eq. (5) with a *surrogate score* in our training objective of Eq. (6) on $SE(3)$, defined as:

$$\tilde{s}_X(\tilde{X}, \sigma) \triangleq -\frac{1}{\sigma^2}z. \quad (13)$$

The detailed training and sampling procedures are available in our supplemental material.

4.4 Proposed Framework

Fig. 3 (left) presents an overview of our proposed framework, comprising a multi-layer perceptron (MLP) cascaded with multiple MLP blocks. This structure is inspired by recent conditional generative models [12, 11], while we modify their approach by substituting linear layers for convolutional ones to condition image generation. The score model processes noisy poses as input and provides estimated scores as output, both represented in a vector form of corresponding lie algebra space of the poses. To extend the score model’s applicability to the image domain, we utilize a ResNet [26] for extracting feature embeddings from input images and encode the time index i using positional embedding [27]. Our score models then condition on image and time features in an interleaved fashion. We found that a single repetition of the MLP block was sufficient in our experimental settings. This architecture enables separation of image feature extractors from our score models, obviating the need for forwarding in every denoising step and thereby significantly enhancing inference speed.

Regarding the design of the conditioning mechanism, a few previous works [12, 11] employ scale-bias condition, which is formulated as $f(x, c) = \mathbf{A}(c)x + \mathbf{B}(c)$. Nevertheless, our empirical observations suggest that this conditioning mechanism does not perform well on learning distributions on $SO(3)$. We hypothesize that this is attributable to the lack of expressivity of the neural networks. Inspired by [28, 29], we propose a new Fourier-based conditioning mechanism, which is formulated as follows:

$$f_i(x, c) = \sum_{j=0}^{d-1} \mathbf{W}_{ij} (\mathbf{A}_j(c) \cos(\pi x_j) + \mathbf{B}_j(c) \sin(\pi x_j)) \quad (14)$$

where d is the dimension of our linear layer. This form bears similarity to the Fourier series $f(t) = \sum_{k=0}^{\infty} \mathbf{A}_k \cos\left(\frac{2\pi k t}{P}\right) + \mathbf{B}_k \sin\left(\frac{2\pi k t}{P}\right)$. Our motivation stems from the fact that the pose distribution on $SO(3)$ is circular, and can therefore be represented as periodic functions. By the definition of periodic functions, their derivatives are also periodic. It is worth noting that this conditioning does not introduce additional parameters in our neural network design, as \mathbf{W}_{ij} is provided by the subsequent linear layer. Our experimental findings suggest that this conditioning scheme enhances the ability of neural network to capture periodic features of score fields on $SO(3)$.

Table 1: Evaluation results on SYMSOL.

Methods	SYMSOL (Spread ↓)					
	Avg.	tet.	cube	icos.	cone	cyl.
DBN [3]	22.44	16.7	40.7	29.5	10.1	15.2
Implicit-PDF [4]	3.96	4.6	4.0	8.4	1.4	1.4
HyperPosePDF [9]	1.94	3.27	2.18	3.24	0.55	0.48
Ours (ResNet34)	0.42	0.43	0.44	0.52	0.35	0.35
Ours (ResNet50)	0.37	0.28	0.32	0.4	0.53	0.31

Table 2: Evaluation results on SYMSOL-T.

Methods	SYMSOL-T (Spread ↓)						
	tet.	cube	icos.	cone	cyl.		
R	t	R	t	R	t	R	
Regression	2.92	0.064	2.86	0.05	2.46	0.037	1.84
Iterative regression	4.25	0.048	4.2	0.037	29.33	0.026	1.63
Ours ($R^3SO(3)$)	1.38	0.017	1.93	0.010	29.35	0.009	1.33
Ours ($SE(3)$)	0.59	0.016	0.58	0.011	0.64	0.012	0.54
							0.41
							0.011

5 Experimental Results

5.1 Experimental Hypotheses and Validation Objectives

Before diving into our experimental findings, we outline our hypotheses. This prepares the ground for understanding the significance of our method and its implications for 6D object pose estimation.

1. *Applicability of Score-based Diffusion Model in the Image Domain:* Our first hypothesis postulates that the score-based diffusion model can be effectively applied in the image domain to address the pose ambiguity issue prevalent in 6D object pose estimation tasks.
2. *Advantage of $SE(3)$ parametrization over $R^3SO(3)$:* We hypothesize that the $SE(3)$ parametrization can offer a comprehensive representation of the joint distribution of object rotation and translation, thus providing an advantage over the $R^3SO(3)$ parametrization.
3. *Mitigation of Perspective Effect Ambiguity through $SE(3)$ parametrization:* We posit that the $SE(3)$ parametrization may alleviate the ambiguity introduced by image perspective effects, a significant challenge in accurate pose estimation, as described in Section 1.
4. *Efficacy of Surrogate Stein Score Formulation on $SE(3)$:* We hypothesize that our surrogate Stein score formulation on $SE(3)$ exhibits improved convergence in Langevin Dynamics compared to the original Stein score computed using automatic differentiation. This aims to confirm the robustness and efficacy of our proposed method amidst complex dynamics.

5.2 Experimental Setups

5.2.1 Datasets and Baselines

In our experiments, we utilize two synthetic datasets: SYMSOL and SYMSOL-T. These datasets serve to examine the effectiveness of our density estimators in different spaces and to benchmark our performance against existing baselines. Additional details are offered in the supplementary material.

SYMSOL. SYMSOL is a dataset specifically designed for evaluating density estimators in the $SO(3)$ space. This dataset, first introduced by [4], comprises 250k images of five texture-less, symmetric 3D objects, with each subject to random rotations. The objects include tetrahedron (tet.), cube, icosahedron (icos.), cone, and cylinder (cyl.), and each exhibits unique symmetries which introduce various degrees of pose ambiguity. For this dataset, we compare our score model on the $SO(3)$ space with several recent works [3, 4, 9]. The baseline models we compare with utilize a pre-trained ResNet50 [30] as their backbones. For the purpose of comparison, we additionally include prior diffusion models [15, 16] in our evaluation within the $SO(3)$ context of our framework. Please note that our work is the first to pioneer the exploration of diffusion models on the SYMSOL dataset.

SYMSOL-T. To extend our evaluation into the $SE(3)$ space, we developed the SYMSOL-T dataset, which is derived from SYMSOL. This new dataset further incorporates random translations, and therefore introduces an additional layer of complexity due to perspective-induced ambiguity. Similar to SYMSOL, it features the same five symmetric shapes and the same number of random samples. For SYMSOL-T, we benchmark our proposed methods against two pose regression methods. These two methods are trained using a symmetry-aware loss function, but with different estimation strategies: one directly estimates the pose from an image, while the other employs iterative refinement.

5.3 Quantitative Results on SYMSOL

In this section, we present the quantitative results evaluated on SYMSOL, and compare our diffusion-based methods with non-parametric ones. We assess the performance of our score model on $SO(3)$

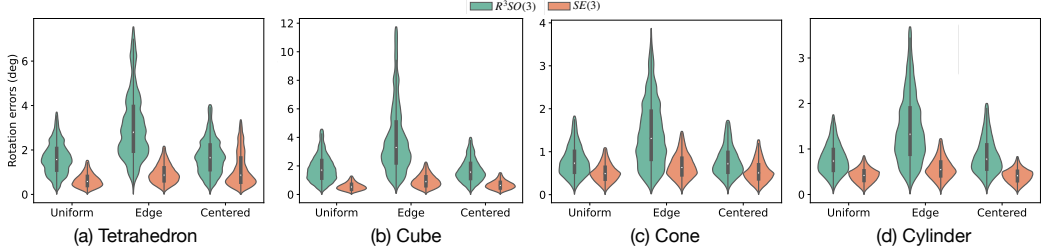


Figure 4: The distribution of angular errors of the $SE(3)$ and $R^3SO(3)$ score models with three configurations and four shapes, in which the width represents the density of data points at a particular range. Please note that the results of $R^3SO(3)$ on *icos*. are not reported as this model fails to adequately handle this particular shape.

across various shapes using both ResNet34 and ResNet50 as the backbones, with the results reported in Table 1. Our model demonstrates promising performance, consistently surpassing the contemporary non-parametric baseline models. It is observed that our model, even when based on the less complex ResNet34 backbone, is still able to achieve results that exceed those of the other baselines using the more complex ResNet50 backbone. The average angular errors are consistently below 1 degree across all shape categories. The performance further improves when employing ResNet50, which emphasizes the potential robustness and scalability of using diffusion models for addressing the pose ambiguity problem. However, it is important to observe that our model with ResNet50 exhibits a slightly reduced performance for the cone shape compared to the ResNet34 variant. This discrepancy can be attributed to our practice of training a single model across all shapes, a strategy that parallels those adopted by Implicit-PDF [4] and HyperPosePDF [9]. Such an approach may lead to mutual influences among shapes with diverse pose distributions, and potentially compromise optimal performance for certain shapes. This observation highlights opportunities for future improvements to our model, specifically in enhancing its ability to effectively learn from data spanning various domains. The endeavors would potentially address the diverse complexities associated with distinct shape and pose characteristics.

5.4 Quantitative Results on SYMSOL-T

In this section, we report the quantitative results obtained from the SYMSOL-T dataset evaluation, as shown in Table 2. The results reveal that our $SE(3)$ and $R^3SO(3)$ score models outperform the pose regression and iterative regression baselines in terms of estimation accuracy. However, the $R^3SO(3)$ score model encounters difficulty when learning the distribution of the icosahedron shape. In contrast, our $SE(3)$ score model excels in estimating rotation across all shapes and achieves competitive results in translation compared to the $R^3SO(3)$ score model, thus demonstrating its ability to model the joint distribution of rotation and translation. Please note that the $SE(3)$ and $R^3SO(3)$ score models do not rely on symmetry annotations, which distinguish them from the pose regression and iterative regression baselines that leverage symmetry supervision. This supports our initial hypothesis that score models are capable of addressing the pose ambiguity problem in the image domain. In the comparison between the $R^3SO(3)$ score model and iterative regression, both models employ iterative refinement. However, our $R^3SO(3)$ score model consistently outperforms iterative regression on tetrahedron, cube, cone, and cylinder shapes. The key difference is that iterative regression focuses on minimizing pose errors without explicitly learning the underlying true distributions. In contrast, our $R^3SO(3)$ score model captures different scales of noise, enabling it to learn the true distribution of pose uncertainty and achieve more accurate results. Regarding translation performance, the $R^3SO(3)$ score model takes the lead over the $SE(3)$ score model. The former's performance can be credited to its assumption of independence between rotation and translation, which effectively eliminates mutual interference. On the other hand, the $SE(3)$ score model learns the joint distribution of rotation and translation, which leads to more robust rotation estimations. The observations therefore support our second hypothesis that $SE(3)$ can provide a more comprehensive pose estimation than $R^3SO(3)$.

5.5 Analysis of $SE(3)$ and $R^3SO(3)$ in the Presence of Image Perspective Ambiguity

To delve deeper into the effects of image perspective on our pose estimation methods, we additionally synthesized three variants of the SYMSOL-T dataset: *Uniform*, *Edge*, and *Centered*. The *Uniform* variant consists of uniformly sampled translations, the *Edge* variant includes translations at the maximum distance from the center, and the *Centered* variant comprises zero translations. Fig. 4 showcases a comparison of the evaluation results for these three variants. We present the distributions

Table 3: Evaluation results for various denoising steps applied to score models on $SE(3)$, trained using automatic differentiation and surrogate scores.

Methods	Steps	SYMSOL-T (Spread \downarrow)									
		tet.		cube		icos.		cone		cyl.	
		R	t	R	t	R	t	R	t	R	t
$SE(3)$ -autograd	100	0.60	0.019	0.59	0.012	0.67	0.012	0.58	0.018	0.41	0.012
	50	0.61	0.019	0.61	0.013	0.66	0.013	0.58	0.019	0.41	0.013
	10	2.89	0.102	3.21	0.113	3.24	0.113	3.12	0.104	3.16	0.108
	5	12.93	0.418	13.07	0.407	10.33	0.302	10.83	0.377	10.09	0.345
$SE(3)$ -surrogate	100	0.59	0.016	0.58	0.011	0.64	0.012	0.55	0.016	0.41	0.011
	50	0.56	0.017	0.58	0.011	0.65	0.012	0.54	0.017	0.41	0.011
	10	0.63	0.017	0.70	0.012	1.71	0.015	0.56	0.019	0.43	0.014
	5	1.22	0.024	2.00	0.028	5.31	0.048	0.72	0.035	0.62	0.031

of angular errors made by the $SE(3)$ and $R^3SO(3)$ score models on these dataset variants and four shapes: tetrahedron, cube, cone, and cylinder. These distributions of angular errors depict the uncertainty of the pose estimations. In line with our hypothesis, the *Edge* variant, which is most influenced by image perspective, exhibits greater uncertainty compared to the *Centered* variant. The *Uniform* variant situates itself between these two. It is evident that both the $R^3SO(3)$ and $SE(3)$ score models demonstrate higher uncertainty on the *Edge* dataset across all shapes, with reduced uncertainty on the *Centered* dataset. The $SE(3)$ score model demonstrates an impressive ability to counter the pose ambiguity introduced by image perspective, a capability that becomes evident when compared with the $R^3SO(3)$ score model. The observation therefore confirms our third hypothesis that $SE(3)$ does exhibit greater robustness to the ambiguity caused by the image perspective issue.

5.6 Performance Analysis: Surrogate Score versus Automatically Differentiated True Score

To test our hypothesis concerning convergence speed, we compare two versions of our score model. The first version, termed $SE(3)$ -surrogate, is trained with the *surrogate score* described in Eq. (13). The second version, termed as $SE(3)$ -autograd, is trained with the *true score* described in Eq. (5) and calculated by automatic differentiation. We trained both estimators and evaluated their performance using different steps of Langevin dynamics. The results are reported in Table 3. Our findings show that when a larger number of Langevin steps (e.g., 100 steps) are used, both score models produce comparable results. However, the performance of $SE(3)$ -autograd significantly declines in comparison to $SE(3)$ -surrogate when the number of sampling steps decreases from 50 to 10 and then to 5. This performance drop is due to the curved manifold represented by the $SE(3)$ parametrization, which can result in the score vector not consistently pointing towards the noise-free data. These results substantiate our fourth hypothesis, and suggest that the application of the *surrogate score* can lead to faster convergence than the use of the *true score* calculated through automatic differentiation.

5.7 Comparison with Other Diffusion Models

In this experiment, we further compare our $SO(3)$ score model with the diffusion models proposed by [15] and [16] using the SYMSOL dataset. While these studies do not specifically address object pose estimation, we have adapted their methods to fit within our framework. The authors of [15] extend the DDPM [12] to $SO(3)$ using an analogy approach, while the authors of [16] reformulate the SGM [11] to apply it to the $SO(3)$ space. The results of these comparisons are presented in Table 4. Our analysis shows that, when excluding Fourier-based conditioning, our diffusion models achieve comparable results across different shapes. However, when Fourier-based conditioning is incorporated, performance significantly improves for three out of the five shapes. This suggests that Fourier-based conditioning enhances the our model’s ability to learn pose distributions.

6 Conclusion

In this paper, we presented a novel approach that applies diffusion models to the $SE(3)$ group for object pose estimation, effectively addressing the pose ambiguity issue. Inspired by the correlation

Table 4: Comparison with diffusion-based approaches.

Methods	SYMSOL (Spread \downarrow)					
	Avg.	tet.	cube	icos.	cone	cyl.
Leach <i>et al.</i> [15]	0.57	0.63	0.54	0.77	0.51	0.38
Jagvaral <i>et al.</i> [16]	1.18	0.52	0.77	3.97	0.32	0.32
Ours w/o fourier	0.89	0.48	0.46	2.86	0.33	0.34
Ours	0.42	0.43	0.44	0.52	0.35	0.35

between rotation and translation distributions caused by image projection effects, we jointly estimated their distributions on $SE(3)$ for improved accuracy. This is the first work to apply diffusion models to $SE(3)$ in the image domain. To validate it, we developed the SYMSOL-T dataset, which enriches the original SYMSOL dataset with randomly sampled translations. Our experiments confirmed the applicability of score-based diffusion models in the image domain, the advantage of $SE(3)$ parametrization over $R^3SO(3)$, and the mitigation of perspective effect ambiguity through $SE(3)$ parametrization. Moreover, our surrogate Stein score formulation on $SE(3)$ exhibited improved convergence in Langevin Dynamics, validating its robustness and efficacy in complex dynamics.

References

- [1] Fabian Manhardt, Diego Martín Arroyo, Christian Rupprecht, Benjamin Busam, Tolga Birdal, Nassir Navab, and Federico Tombari. Explaining the ambiguity of object detection and 6d pose from visual data. In *Proc. IEEE Int. Conf. on Computer Vision (ICCV)*, pages 6840–6849, 2019.
- [2] Tomás Hodan, Dániel Baráth, and Jiri Matas. EPOS: estimating 6d pose of objects with symmetries. In *Proc. IEEE Conf. on Computer Vision and Pattern Recognition (CVPR)*, pages 11700–11709, 2020.
- [3] Haowen Deng, Mai Bui, Nassir Navab, Leonidas Guibas, Slobodan Ilic, and Tolga Birdal. Deep bingham networks: Dealing with uncertainty and ambiguity in pose estimation, 2020.
- [4] Kieran A. Murphy, Carlos Esteves, Varun Jampani, Srikumar Ramalingam, and Ameesh Makadia. Implicit-pdf: Non-parametric representation of probability distributions on the rotation manifold. In *Proc. Int. Conf. on Machine Learning (ICML)*, volume 139, pages 7882–7893, 2021.
- [5] Tomáš Hodan, Pavel Haluza, Štepán Obdržálek, Jiri Matas, Manolis Lourakis, and Xenophon Zabulis. T-less: An rgb-d dataset for 6d pose estimation of texture-less objects. In *2017 IEEE Winter Conference on Applications of Computer Vision (WACV)*, pages 880–888. IEEE, 2017.
- [6] Kiru Park, Timothy Patten, and Markus Vincze. Pix2pose: Pixel-wise coordinate regression of objects for 6d pose estimation. In *Proc. IEEE Int. Conf. on Computer Vision (ICCV)*, pages 7667–7676, 2019.
- [7] Gu Wang, Fabian Manhardt, Federico Tombari, and Xiangyang Ji. Gdr-net: Geometry-guided direct regression network for monocular 6d object pose estimation. In *Proc. IEEE Conf. on Computer Vision and Pattern Recognition (CVPR)*, pages 16611–16621, 2021.
- [8] Stefan Thalhammer, Timothy Patten, and Markus Vincze. COPE: end-to-end trainable constant runtime object pose estimation. In *Proc. IEEE Winter Conf. on Applications of Computer Vision (WACV)*, pages 2859–2869, 2023.
- [9] Yixiao Guo, Jiawei Liu, Guo Li, Luo Mai, and Hao Dong. Fast and flexible human pose estimation with hyperpose. In *ACM Int. Conf. on Multimedia*, pages 3763–3766, 2021.
- [10] Rasmus Laurvig Haugaard, Frederik Hagelskjær, and Thorkjørn Mosekjær Iversen. Spyro-pose: Importance sampling pyramids for object pose distribution estimation in $SE(3)$. *CoRR*, abs/2303.05308, 2023.
- [11] Yang Song and Stefano Ermon. Generative modeling by estimating gradients of the data distribution. In *Proc. Conf. on Neural Information Processing Systems (NeurIPS)*, pages 11895–11907, 2019.
- [12] Jonathan Ho, Ajay Jain, and Pieter Abbeel. Denoising diffusion probabilistic models. In *Proc. Conf. on Neural Information Processing Systems (NeurIPS)*, 2020.
- [13] Jiaming Song, Chenlin Meng, and Stefano Ermon. Denoising diffusion implicit models. In *Proc. Int. Conf. on Learning Representations (ICLR)*, 2021.
- [14] Yang Song, Jascha Sohl-Dickstein, Diederik P. Kingma, Abhishek Kumar, Stefano Ermon, and Ben Poole. Score-based generative modeling through stochastic differential equations. In *Proc. Int. Conf. on Learning Representations (ICLR)*, 2021.

[15] Adam Leach, Sebastian M Schmon, Matteo T. Degiacomi, and Chris G. Willcocks. Denoising diffusion probabilistic models on $so(3)$ for rotational alignment. In *Proc. Int. Conf. on Learning Representations Workshop (ICLRW)*, 2022.

[16] Yesukhei Jagvaral, Francois Lanusse, and Rachel Mandelbaum. Diffusion generative models on $so(3)$. <https://openreview.net/pdf?id=jHA-yCyBGb>, 2023.

[17] Julen Urain, Niklas Funk, Jan Peters, and Georgia Chalvatzaki. $Se(3)$ -diffusionfields: Learning smooth cost functions for joint grasp and motion optimization through diffusion. *CoRR*, abs/2209.03855, 2022.

[18] Jason Yim, Brian L. Trippe, Valentin De Bortoli, Emile Mathieu, Arnaud Doucet, Regina Barzilay, and Tommi S. Jaakkola. $SE(3)$ diffusion model with application to protein backbone generation. *CoRR*, abs/2302.02277, 2023.

[19] Joan Solà, Jérémie Deray, and Dinesh Atchuthan. A micro lie theory for state estimation in robotics. *CoRR*, abs/1812.01537, 2018.

[20] Pascal Vincent. A connection between score matching and denoising autoencoders. *Neural Comput.*, 23(7):1661–1674, 2011.

[21] Dmitry I Nikolayev and Tatjana I Savyolov. Normal distribution on the rotation group $so(3)$. *Textures and Microstructures*, 29, 1970.

[22] Salem Said, Lionel Bombrun, Yannick Berthoumieu, and Jonathan H. Manton. Riemannian gaussian distributions on the space of symmetric positive definite matrices. *IEEE Trans. Inf. Theory*, 63(4):2153–2170, 2017.

[23] Gregory Chirikjian and Marin Kobilarov. Gaussian approximation of non-linear measurement models on lie groups. In *53rd IEEE Conference on Decision and Control*, pages 6401–6406. IEEE, 2014.

[24] Valentin De Bortoli, Emile Mathieu, Michael John Hutchinson, James Thornton, Yee Whye Teh, and Arnaud Doucet. Riemannian score-based generative modelling. In Alice H. Oh, Alekh Agarwal, Danielle Belgrave, and Kyunghyun Cho, editors, *Advances in Neural Information Processing Systems*, 2022.

[25] Timothy D. Barfoot and Paul Timothy Furgale. Associating uncertainty with three-dimensional poses for use in estimation problems. *IEEE Trans. Robotics*, 30:679–693, 2014.

[26] Kaiming He, Xiangyu Zhang, Shaoqing Ren, and Jian Sun. Deep residual learning for image recognition. In *Proceedings of the IEEE conference on computer vision and pattern recognition*, pages 770–778, 2016.

[27] Ashish Vaswani, Noam Shazeer, Niki Parmar, Jakob Uszkoreit, Llion Jones, Aidan N Gomez, Łukasz Kaiser, and Illia Polosukhin. Attention is all you need. *Advances in neural information processing systems*, 30, 2017.

[28] Liu Ziyin, Tilman Hartwig, and Masahito Ueda. Neural networks fail to learn periodic functions and how to fix it. *Advances in Neural Information Processing Systems*, 33:1583–1594, 2020.

[29] Jiyoung Lee, Wonjae Kim, Daehoon Gwak, and Edward Choi. Conditional generation of periodic signals with fourier-based decoder. *arXiv preprint arXiv:2110.12365*, 2021.

[30] Kaiming He, Xiangyu Zhang, Shaoqing Ren, and Jian Sun. Deep residual learning for image recognition. In *Proc. IEEE Conf. on Computer Vision and Pattern Recognition (CVPR)*, pages 770–778, 2016.

[31] James Bradbury, Roy Frostig, Peter Hawkins, Matthew James Johnson, Chris Leary, Dougal Maclaurin, George Necula, Adam Paszke, Jake VanderPlas, Skye Wanderman-Milne, and Qiao Zhang. JAX: composable transformations of Python+NumPy programs, 2018.

[32] Brent Yi, Michelle Lee, Alina Kloss, Roberto Martín-Martín, and Jeannette Bohg. Differentiable factor graph optimization for learning smoothers. In *2021 IEEE/RSJ International Conference on Intelligent Robots and Systems (IROS)*, 2021.

[33] Diederick P Kingma and Jimmy Ba. Adam: A method for stochastic optimization. In *Proc. Int. Conf. on Learning Representations (ICLR)*, 2015.

[34] Yu Xiang, Tanner Schmidt, Venkatraman Narayanan, and Dieter Fox. Posecnn: A convolutional neural network for 6d object pose estimation in cluttered scenes. In *Robotics: Science and Systems XIV*, 2018.

[35] Arash Amini, Arul Selvam Periyasamy, and Sven Behnke. Yolopose: Transformer-based multi-object 6d pose estimation using keypoint regression. In *Intelligent Autonomous Systems (IAS)*, volume 577, pages 392–406, 2022.

[36] Yann Labb  , Justin Carpentier, Mathieu Aubry, and Josef Sivic. Cosopose: Consistent multi-view multi-object 6d pose estimation. In *Computer Vision–ECCV 2020: 16th European Conference, Glasgow, UK, August 23–28, 2020, Proceedings, Part XVII 16*, pages 574–591. Springer, 2020.

[37] Yan Di, Fabian Manhardt, Gu Wang, Xiangyang Ji, Nassir Navab, and Federico Tombari. So-pose: Exploiting self-occlusion for direct 6d pose estimation. In *Proc. IEEE Int. Conf. on Computer Vision (ICCV)*, pages 12376–12385, 2021.

[38] Sida Peng, Yuan Liu, Qixing Huang, Xiaowei Zhou, and Hujun Bao. Pvnet: Pixel-wise voting network for 6dof pose estimation. In *Proc. IEEE Conf. on Computer Vision and Pattern Recognition (CVPR)*, pages 4561–4570, 2019.

[39] Mahdi Rad and Vincent Lepetit. BB8: A scalable, accurate, robust to partial occlusion method for predicting the 3d poses of challenging objects without using depth. In *Proc. IEEE Int. Conf. on Computer Vision (ICCV)*, pages 3848–3856, 2017.

[40] He Wang, Srinath Sridhar, Jingwei Huang, Julien Valentin, Shuran Song, and Leonidas J Guibas. Normalized object coordinate space for category-level 6d object pose and size estimation. In *Proceedings of the IEEE/CVF Conference on Computer Vision and Pattern Recognition*, pages 2642–2651, 2019.

[41] Lin Huang, Tomas Hodan, Lingni Ma, Linguang Zhang, Luan Tran, Christopher D. Twigg, Po-Chen Wu, Junsong Yuan, Cem Keskin, and Robert Wang. Neural correspondence field for object pose estimation. In *Proc. European Conf. on Computer Vision (ECCV)*, volume 13670, pages 585–603, 2022.

[42] Brian Okorn, Mengyun Xu, Martial Hebert, and David Held. Learning orientation distributions for object pose estimation. In *2020 IEEE/RSJ International Conference on Intelligent Robots and Systems (IROS)*, pages 10580–10587. IEEE, 2020.

[43] Igor Gilitschenski, Roshni Sahoo, Wilko Schwarting, Alexander Amini, Sertac Karaman, and Daniela Rus. Deep orientation uncertainty learning based on a bingham loss. In *International conference on learning representations*, 2020.

[44] Sergey Prokudin, Peter Gehler, and Sebastian Nowozin. Deep directional statistics: Pose estimation with uncertainty quantification. In *Proceedings of the European conference on computer vision (ECCV)*, pages 534–551, 2018.

[45] David M Klee, Ondrej Biza, Robert Platt, and Robin Walters. Image to sphere: Learning equivariant features for efficient pose prediction. *arXiv preprint arXiv:2302.13926*, 2023.

[46] Ling Yang, Zhilong Zhang, Yang Song, Shenda Hong, Runsheng Xu, Yue Zhao, Yingxia Shao, Wentao Zhang, Bin Cui, and Ming-Hsuan Yang. Diffusion models: A comprehensive survey of methods and applications. *arXiv preprint arXiv:2209.00796*, 2022.

[47] Aditya Ramesh, Prafulla Dhariwal, Alex Nichol, Casey Chu, and Mark Chen. Hierarchical text-conditional image generation with clip latents. *arXiv preprint arXiv:2204.06125*, 2022.

[48] Nataniel Ruiz, Yuanzhen Li, Varun Jampani, Yael Pritch, Michael Rubinstein, and Kfir Aberman. Dreambooth: Fine tuning text-to-image diffusion models for subject-driven generation. *arXiv preprint arXiv:2208.12242*, 2022.

[49] Robin Rombach, Andreas Blattmann, Dominik Lorenz, Patrick Esser, and Björn Ommer. High-resolution image synthesis with latent diffusion models. In *Proceedings of the IEEE/CVF Conference on Computer Vision and Pattern Recognition*, pages 10684–10695, 2022.

[50] Chitwan Saharia, William Chan, Saurabh Saxena, Lala Li, Jay Whang, Emily L Denton, Kamyar Ghasemipour, Raphael Gontijo Lopes, Burcu Karagol Ayan, Tim Salimans, et al. Photorealistic text-to-image diffusion models with deep language understanding. *Advances in Neural Information Processing Systems*, 35:36479–36494, 2022.

[51] Ruihan Yang, Prakhar Srivastava, and Stephan Mandt. Diffusion probabilistic modeling for video generation. *arXiv preprint arXiv:2203.09481*, 2022.

[52] Jonathan Ho, Tim Salimans, Alexey Gritsenko, William Chan, Mohammad Norouzi, and David J Fleet. Video diffusion models. *arXiv preprint arXiv:2204.03458*, 2022.

[53] Jonathan Ho, William Chan, Chitwan Saharia, Jay Whang, Ruiqi Gao, Alexey Gritsenko, Diederik P Kingma, Ben Poole, Mohammad Norouzi, David J Fleet, et al. Imagen video: High definition video generation with diffusion models. *arXiv preprint arXiv:2210.02303*, 2022.

[54] Rongjie Huang, Zhou Zhao, Huadai Liu, Jinglin Liu, Chenye Cui, and Yi Ren. Prodif: Progressive fast diffusion model for high-quality text-to-speech. In *Proceedings of the 30th ACM International Conference on Multimedia*, pages 2595–2605, 2022.

[55] Dongchao Yang, Jianwei Yu, Helin Wang, Wen Wang, Chao Weng, Yuexian Zou, and Dong Yu. Diffsound: Discrete diffusion model for text-to-sound generation. *IEEE/ACM Transactions on Audio, Speech, and Language Processing*, 2023.

[56] Shansan Gong, Mukai Li, Jiangtao Feng, Zhiyong Wu, and LingPeng Kong. Diffuseq: Sequence to sequence text generation with diffusion models. *arXiv preprint arXiv:2210.08933*, 2022.

[57] Xiang Li, John Thickstun, Ishaan Gulrajani, Percy S Liang, and Tatsunori B Hashimoto. Diffusion-lm improves controllable text generation. *Advances in Neural Information Processing Systems*, 35:4328–4343, 2022.

[58] Florinel-Alin Croitoru, Vlad Hondru, Radu Tudor Ionescu, and Mubarak Shah. Diffusion models in vision: A survey. *IEEE Transactions on Pattern Analysis and Machine Intelligence*, 2023.

[59] Tomer Amit, Tal Shaharbany, Eliya Nachmani, and Lior Wolf. Segdiff: Image segmentation with diffusion probabilistic models. *arXiv preprint arXiv:2112.00390*, 2021.

[60] Dmitry Baranchuk, Ivan Rubachev, Andrey Voynov, Valentin Khrulkov, and Artem Babenko. Label-efficient semantic segmentation with diffusion models. *arXiv preprint arXiv:2112.03126*, 2021.

[61] Shoufa Chen, Peize Sun, Yibingimp Song, and Ping Luo. Diffusiondet: Diffusion model for object detection. *CoRR*, abs/2211.09788, 2022.

[62] Jeongjun Choi, Dongseok Shim, and H. Jin Kim. Diffupose: Monocular 3d human pose estimation via denoising diffusion probabilistic model. *CoRR*, abs/2212.02796, 2022.

[63] Karl Holmquist and Bastian Wandt. Diffpose: Multi-hypothesis human pose estimation using diffusion models. *arXiv preprint arXiv:2211.16487*, 2022.

[64] Erik Jørgensen. The central limit problem for geodesic random walks. *Zeitschrift für Wahrscheinlichkeitstheorie und verwandte Gebiete*, 32(1-2):1–64, 1975.

[65] Tomáš Hodaň, Martin Sundermeyer, Bertram Drost, Yann Labb  , Eric Brachmann, Frank Michel, Carsten Rother, and Ji   Matas. Bop challenge 2020 on 6d object localization. In *Computer Vision–ECCV 2020 Workshops: Glasgow, UK, August 23–28, 2020, Proceedings, Part II 16*, pages 577–594. Springer, 2020.

Supplementary Material

In this supplementary material, we first present additional details of our experimental designs in Section A. This is followed by providing the proofs of our Stein score calculation in Section B. In Section C, we review the previous works relevant to our paper. Finally, in Section D, we discuss the limitations and broader impacts of our work.

A Additional Experimental Details

A.1 Calculation of Stein Scores Using Automatic Differentiation in JAX

As stated by [16], the Stein scores can be computed as follows:

$$\nabla_Y \log p_{\Sigma}(Y|X) = \frac{\partial}{\partial k} \log p_{\Sigma}(Y \text{Exp}(k\tau)|X) \Big|_{k=0}, \quad (15)$$

where $k \in \mathbb{R}$, $\tau \in \mathfrak{g}$, $k\tau$ indicates a small perturbation on \mathcal{G} . In practice, this can be computed by automatic differentiation. In the following code snippet, we demonstrate our implementation based on JAX [31] and *jaxlie* [32].

```
from jaxlie import S03, SE3
import jax
import jax.numpy as jnp

Lie = S03  # Specify Lie groups

# geodesic distance
def geodesic(y, x):
    return jnp.linalg.norm(
        x.inverse() @ y).log()

# log-Gaussian distribution Eq. (3)
def log_gauss(y, x, sigma=1.0):
    return -0.5 * geodesic(y, x) ** 2 / sigma**2

# Eq. (25)
def calc_score(y, x, sigma=1.0):
    return jax.grad(
        lambda tau: log_gauss(
            Lie.exp(y) @ Lie.exp(tau),
            Lie.exp(x),
            sigma
        )
    )(jnp.zeros(Lie.tangent_dim))  # 3 for S03, 6 for SE3
```

Listing 1: Calculation of Stein scores using automatic differentiation

A.2 Algorithms

The algorithms used for our training and sampling procedures are presented in Algorithms 1 and 2, respectively. The notations employed conform to those detailed in the main manuscript.

A.3 Datasets

The SYMSOL-T dataset contains 250k images of five symmetric, texture-less three-dimensional objects. Following the structure of SYMSOL [4], each shape has 45k training images and 5k testing images. The dataset ensures that translations over the x , y , and z axes are uniformly sampled within the range of $[-1, 1]$. In the experiments examining image perspective ambiguity in Section 5.5, each of the dataset variants (i.e., *Uniform*, *Edge*, and *Centered*) comprises 200 images per shape. Our analysis is performed based on 1k randomly generated poses from our score models for each image.

Algorithm 1: Training Score Model on $SE(3)$

```

Require:  $s_\theta, \{\sigma_i\}_{i=0}^L, p_{\text{data}}$ 
for  $j \in \{0, \dots, N_{\text{iter}} - 1\}$  do
|  $i \sim \mathcal{U}(0, L - 1)$ 
|  $X \sim p_{\text{data}}(X)$ 
|  $\tilde{X} = X \text{Exp}(z), z \sim \mathcal{N}(0, \sigma_i^2 I)$ 
|  $\ell_\theta = \|s_\theta(\tilde{X}, \sigma_i) - \tilde{s}_X(\tilde{X}, \sigma_i)\|_2^2$ 
|  $\theta \leftarrow \text{optimize}(\theta, \ell_\theta)$ 
end

```

Algorithm 2: Sampling (Langevin Dynamics on \mathcal{G})

```

Require:  $s_\theta, \{\sigma_i\}_{i=0}^L, \{\epsilon_i\}_{i=0}^L, \tilde{X}_0$ 
for  $i \in \{0, \dots, L - 1\}$  do
|  $z_i \sim \mathcal{N}(0, I)$ 
|  $\tilde{X}_{i+1} = \tilde{X}_i \text{Exp}(\epsilon_i s_\theta(\tilde{X}_i, \sigma_i) + \sqrt{2\epsilon_i} z_i^m)$ 
end
return  $\tilde{X}_L$ 

```

A.4 Hyperparameters

In our experiments, we utilize a pre-trained ResNet34 model [30] as the standard backbone across all methods, unless explicitly stated otherwise. In the SYMSOL experiments, we select 16 different clean samples in each iteration. Each of these samples is perturbed to generate 256 different noisy variants, resulting in a total of 4,096 noisy samples. The proposed score-based model is then trained for 400k steps to denoise these samples. In the SYMSOL-T experiments, the pose regression approach is trained for 400k steps. Meanwhile, the iterative regression and both our $R^3 SO(3)$ and $SE(3)$ score models are subjected to an extended training duration of 800k steps. We employ the Adam optimizer [33] with an initial learning rate set at 10^{-4} . During the latter half of the training schedule, we apply an exponential decay, which lowers the learning rate to 10^{-5} . For the diffusion process, we use a linear noise scheduling approach that ranges from 10^{-4} to 1.0, divided into 100 discrete steps.

Table 5: Hyperparameters.

Hyperparameters	SYMSOL	SYMSOL-T
Learning rate	$[10^{-4}, 10^{-5}]$	$[10^{-4}, 10^{-5}]$
Batch size	16	16
Number of noisy samples	256	256
Training steps	400k	800k
Optimizer	Adam	Adam
Noise scale	$[10^{-4}, 1.0]$	$[10^{-4}, 1.0]$
Denoising steps	100	100
Number of MLP blocks	1	1

A.5 Evaluation Metrics

In our experiments, we employ two evaluation metrics to assess the accuracy of the estimated poses. In the SYMSOL experiments, we adopt the minimum angular distance, measured in degrees, between a set of ground truth equivalent rotations and the estimated rotations as the evaluation metric. For the SYMSOL-T experiments, we incorporate the Euclidean distance between the ground truth and the estimated translations as our metric to evaluate the accuracy of translation. Each of these distance metrics is computed per sample, and we report their averages over all samples in our results. These two evaluation metrics allow us to verify the quality of the poses estimated by our proposed method.

A.6 Visualization of SYMSOL-T Results

In Fig 5, we present the SYMSOL-T results obtained from our $SE(3)$ score model for each shape. The model predictions are displayed in green and correlate to the corresponding original input images that are illustrated in gray. To visualize the density predictions, we adopt the strategy employed in [4] to represent the rotation and translation densities generated by our model in the $SO(3)$ and \mathbb{R}^3 spaces, respectively. Specifically, we use the Mollweide projection for visualizing the $SO(3)$ space, with longitude and latitude values representing the yaw and pitch of the object’s rotation, respectively. The color in the $SO(3)$ space indicates the roll of the object’s rotation. In the \mathbb{R}^3 space, the (R, G, B) color channels are utilized to represent the 3D coordinates (x, y, z) . Within the plots, the circles denote sets of equivalent poses, with each dot representing a single sample. For each plot, We generate a total of 1,000 random samples from our model. Please note that both the cone and the cylinder exhibit continuous symmetries. This causes the circles on $SO(3)$ to overlap densely and

connect, which gives rise to tilde shapes on the sphere. In the case of \mathbb{R}^3 , a single circle is present due to the unique solution for the translation. The samples generated from our score model are tightly concentrated in the center of each circle. This evidence highlights the capability of our model to accurately capture equivalent object poses originating from either discrete or continuous symmetries.

B Proofs

B.1 Closed-form of Stein scores

In this section, we present the derivation of the closed-form solution for the Stein scores. We begin with a revisit of the Gaussian distribution on the Lie group \mathcal{G} , which is formulated as follows:

$$p_{\Sigma}(Y|X) := \mathcal{N}_{\mathcal{G}}(Y; X, \Sigma) \triangleq \frac{1}{\zeta(\Sigma)} \exp\left(-\frac{1}{2} \text{Log}(X^{-1}Y)^{\top} \Sigma^{-1} \text{Log}(X^{-1}Y)\right). \quad (16)$$

To derive Eq. (4), we utilize the definition of Stein scores, which is defined as the derivative of log-density of the data distribution with respect to the group element $Y \in \mathcal{G}$, expressed as follows:

$$\begin{aligned} \nabla_Y \log p_{\Sigma}(Y|X)^{\top} &= \frac{\partial}{\partial Y} \left(-\frac{1}{2} \text{Log}(X^{-1}Y)^{\top} \Sigma^{-1} \text{Log}(X^{-1}Y) \right) \\ &= \frac{\partial}{\partial \text{Log}(X^{-1}Y)} \left(-\frac{1}{2} \text{Log}(X^{-1}Y)^{\top} \Sigma^{-1} \text{Log}(X^{-1}Y) \right) \frac{\partial \text{Log}(X^{-1}Y)}{\partial Y} \\ &= -\text{Log}(X^{-1}Y)^{\top} \Sigma^{-1} \left(\frac{\partial \text{Log}(X^{-1}Y)}{\partial (X^{-1}Y)} \cdot \frac{\partial (X^{-1}Y)}{\partial Y} \right) \\ &= -\text{Log}(X^{-1}Y)^{\top} \Sigma^{-1} (\mathbf{J}_r^{-1}(\text{Log}(X^{-1}Y)) \cdot I) \\ &= -\text{Log}(X^{-1}Y)^{\top} \Sigma^{-1} \mathbf{J}_r^{-1}(\text{Log}(X^{-1}Y)). \end{aligned} \quad (17)$$

Based on the above derivation, the closed-form solution for the Stein scores is obtained as follows:

$$\nabla_Y \log p_{\Sigma}(Y|X) = -\mathbf{J}_r^{-\top}(\text{Log}(X^{-1}Y)) \Sigma^{-1} \text{Log}(X^{-1}Y). \quad (18)$$

B.2 Left and Right Jacobians on $SO(3)$

In this section, we present the derivation of Eq. (8). Let $z = [z_x, z_y, z_z] \in \mathfrak{so}(3)$ and $\phi = \|z\|_2^2$. The skew-symmetric matrix induced by z can therefore be represented as follows:

$$z_{\times} = \begin{bmatrix} 0 & -z_z & z_y \\ z_z & 0 & -z_x \\ -z_y & z_x & 0 \end{bmatrix} \quad (19)$$

As demonstrated in [19], the left and the right Jacobian on $SO(3)$ can be expressed as the following closed-form expressions:

$$\begin{aligned} \mathbf{J}_r(z) &= I - \frac{1 - \cos \phi}{\phi^2} z_{\times} + \frac{\phi - \sin \phi}{\phi^3} z_{\times}^2 \\ \mathbf{J}_r^{-1}(z) &= I + \frac{1}{2} z_{\times} + \left(\frac{1}{\phi} - \frac{1 + \cos \phi}{2\phi \sin \phi} \right) z_{\times}^2 \\ \mathbf{J}_l(z) &= I + \frac{1 - \cos \phi}{\phi^2} z_{\times} + \frac{\phi - \sin \phi}{\phi^3} z_{\times}^2 \\ \mathbf{J}_l^{-1}(z) &= I - \frac{1}{2} z_{\times} + \left(\frac{1}{\phi} - \frac{1 + \cos \phi}{2\phi \sin \phi} \right) z_{\times}^2. \end{aligned} \quad (20)$$

As a result, Eq. (8) of the main manuscript can be derived as follow:

$$\mathbf{J}_l(z) = \mathbf{J}_r^{\top}(z), \quad \mathbf{J}_l^{-1}(z) = \mathbf{J}_r^{-\top}(z). \quad (21)$$

B.3 Eigenvector of The Jacobians

For the purpose of proving Eq. (9), we consider the derivative of exponential mapping on \mathcal{G} , where $k \in \mathbb{R}$ and $z \in \mathfrak{g}$. More specifically, by applying the chain rule on the derivative of the small perturbation $\text{Exp}(kz)$ on \mathcal{G} with respect to k , we can obtain the resultant equation as follows:

$$\frac{\partial \text{Exp}(kz)}{\partial k} = \frac{\partial \text{Exp}(kz)}{\partial (kz)} \frac{\partial (kz)}{\partial k} = \mathbf{J}_l(kz)z. \quad (22)$$

On the other hand, by applying the differential rule, the following equations can be derived:

$$\begin{aligned} \frac{\partial \text{Exp}(kz)}{\partial k} &= \lim_{h \rightarrow 0} \frac{\text{Log}(\text{Exp}((k+h)z)\text{Exp}(kz)^{-1})}{k} \\ &= \lim_{h \rightarrow 0} \frac{\text{Log}(\text{Exp}(hz)\text{Exp}(kz)\text{Exp}(kz)^{-1})}{h} = z. \end{aligned} \quad (23)$$

By further combining Eqs. (22) and (23) and setting $k = 1$, the following equation can be derived:

$$\mathbf{J}_l(z)z = z. \quad (24)$$

The resultant Eq. (24) suggests that z is an eigenvector of $\mathbf{J}_l(z)$. Please note that the same rule can also be employed to provide a proof for the right-Jacobian as follows:

$$\mathbf{J}_r(z)z = z. \quad (25)$$

B.4 Closed-Form of Stein Scores on $SE(3)$

In this section, we delve into the closed-form solution of Stein scores on $SE(3)$, which is referenced in Section 4.3. Let $z = (\rho, \phi) \in \mathfrak{se}(3)$, where ρ represents the translational part and ϕ denotes the rotational part. We define $\hat{\phi} = \|\phi\|_2^2$ and recall the inverse of the left-Jacobian on $SE(3)$ as follows:

$$\mathbf{J}_l^{-1}(z) = \begin{bmatrix} \mathbf{J}_l^{-1}(\phi) & \mathbf{Z}(\rho, \phi) \\ 0 & \mathbf{J}_l^{-1}(\phi) \end{bmatrix}, \quad (26)$$

where $\mathbf{Z}(\rho, \phi) = -\mathbf{J}_l^{-1}(\phi)\mathbf{Q}(\rho, \phi)\mathbf{J}_l^{-1}(\phi)$. The complete form of $\mathbf{Q}(\rho, \phi)$ is defined in [19, 25] as:

$$\begin{aligned} \mathbf{Q}(\rho, \phi) &= \frac{1}{2}\rho_{\times} + \frac{\hat{\phi} - \sin \hat{\phi}}{\hat{\phi}^3}(\phi_{\times}\rho_{\times} + \rho_{\times}\phi_{\times} + \phi_{\times}\rho_{\times}\phi_{\times}) \\ &\quad - \frac{1 - \frac{\hat{\phi}^2}{2} - \cos \hat{\phi}}{\hat{\phi}^4}(\phi_{\times}^2\rho_{\times} + \rho_{\times}\phi_{\times}^2 - 3\phi_{\times}\rho_{\times}\phi_{\times}) \\ &\quad - \frac{1}{2} \left(\frac{1 - \frac{\hat{\phi}^2}{2} - \cos \hat{\phi}}{\hat{\phi}^4} - 3\frac{\hat{\phi} - \sin \hat{\phi} - \frac{\hat{\phi}^3}{6}}{\hat{\phi}^5}(\phi_{\times}\rho_{\times}\phi_{\times}^2 + \phi_{\times}^2\rho_{\times}\phi_{\times}) \right). \end{aligned} \quad (27)$$

From the Eq. (27), an essential property can be observed and expressed as follows:

$$\mathbf{Q}^{\top}(-\rho, -\phi) = \mathbf{Q}(\rho, \phi). \quad (28)$$

Based on the above derivation, the closed-form expression of the inverse transposed right-Jacobian on $SE(3)$ combined with the property outlined in Eq. (28) can be derived as follows:

$$\begin{aligned} \mathbf{J}_r^{-\top}(z) &= (\mathbf{J}_l^{-1}(-z))^{\top} \\ &= \begin{bmatrix} \mathbf{J}_l^{-1}(-\phi) & \mathbf{Z}(-\rho, -\phi) \\ 0 & \mathbf{J}_l^{-1}(-\phi) \end{bmatrix}^{\top} \\ &= \begin{bmatrix} \mathbf{J}_r^{-1}(\phi) & -\mathbf{J}_r^{-1}(\phi)\mathbf{Q}(-\rho, -\phi)\mathbf{J}_r^{-1}(\phi) \\ 0 & \mathbf{J}_r^{-1}(\phi) \end{bmatrix}^{\top} \\ &= \begin{bmatrix} \mathbf{J}_r^{-\top}(\phi) & 0 \\ -\mathbf{J}_r^{-\top}(\phi)\mathbf{Q}^{\top}(-\rho, -\phi)\mathbf{J}_r^{-\top}(\phi) & \mathbf{J}_r^{-\top}(\phi) \end{bmatrix} \\ &= \begin{bmatrix} \mathbf{J}_l^{-1}(\phi) & 0 \\ -\mathbf{J}_l^{-1}(\phi)\mathbf{Q}(\rho, \phi)\mathbf{J}_l^{-1}(\phi) & \mathbf{J}_l^{-1}(\phi) \end{bmatrix} \\ &= \begin{bmatrix} \mathbf{J}_l^{-1}(\phi) & 0 \\ \mathbf{Z}(\rho, \phi) & \mathbf{J}_l^{-1}(\phi) \end{bmatrix} \end{aligned} \quad (29)$$

The closed-form solution of Stein score on $SE(3)$ can then be computed by the definition of Stein score as follows:

$$\nabla_Y \log p_\sigma(\tilde{X}|X) = -\frac{1}{\sigma^2} \begin{bmatrix} \mathbf{J}_l^{-1}(\phi) & 0 \\ \mathbf{Z}(\rho, \phi) & \mathbf{J}_l^{-1}(\phi) \end{bmatrix} z. \quad (30)$$

After examining the derivation process, it is clear that this computation involves the costly calculation of Jacobians, and does not confer any computational benefits when using automatic differentiation. However, by adopting the surrogate score presented in Eq. (13), it is possible to reduce the computation of the Jacobian $J_r^{-\top}(z)$, while simultaneously improving performance, as explained in Section 5.6.

C Related Works

C.1 Methodologies for Dealing with Pose Ambiguity Issues

Pose ambiguity remains a significant challenge within the realm of object pose estimation. A variety of strategies have been employed in the literature to explicitly tackle this issue, ranging from the application of symmetry supervisions to the use of surrogate losses [34, 35]. Recent regression-based techniques, such as those presented in [36, 7, 37, 8], strive to minimize the pose discrepancy by seeking the closest candidate within a set of ambiguous poses. Other methods, such as [38, 39], apply constraints to the regression targets, particularly for rotation angles, to mitigate ambiguity. In addition, there are approaches like [6, 40, 41] that propose regressing to a predetermined set of geometric features derived from symmetry annotations. Although these previous methods are able to effectively handle pose ambiguity arising from symmetric objects, they often necessitate manual labeling of equivalent poses.

On the other hand, several studies have investigated methods to model the inherent uncertainty in pose ambiguity. This involves the quantification and representation of uncertainty associated with the estimated poses. Some works have employed parametric distributions such as Bingham distributions [42, 43, 3] and von-Mises distributions [44] to model the orientation uncertainty. There are also approaches, such as in [1], that estimate a Bingham distribution using an ensemble of pose hypotheses. A number of studies [4, 9, 45, 10] have opted to employ non-parametric distributions to implicitly represent rotation uncertainty densities on $SO(3)$. While these methods do not require symmetry annotations, they typically consider rotations and translations as independent factors.

C.2 Previous Diffusion Probabilistic Models and Their Application Domains

Diffusion probabilistic models [46, 12–14, 11] represent a class of generative models designed to learn the underlying probability distribution of data. They have been applied to various generative tasks, and have shown impressive results in several application domains, including image [47–50], video [51–53], audio [54, 55], and natural language processing [56, 57]. Recently, diffusion models have found broader applications in discriminative tasks [58], such as semantic segmentation [59, 60] and object detection [61]. In the realm of human pose estimation, they have been useful in addressing joint location ambiguity stemming from the projection of 2D keypoints into 3D space [62, 63]. Despite the presence of similar challenges in object pose estimation, this area remains relatively unexplored.

While the aforementioned diffusion models primarily operate in Euclidean space, several authors have extended this concept to more complex spaces, such as manifolds, to accommodate data residing on these structures. For instance, the authors in [24] extended diffusion models to Riemannian manifolds, and leveraged Geodesic Random Walk [64] for sampling. Other studies [16, 15] applied the Denoising Diffusion Probabilistic Models (DDPM) [12] and score-based generative models [14, 11] to the $SO(3)$ manifold to recover probability density of data on $SO(3)$. Further extensions of diffusion models to $SE(3)$ have been proposed for tasks such as unfolding protein structures and grasping objects [17, 18]. These approaches typically used a straightforward parametrization on $SE(3)$, and treated rotation and translation as separate entities for diffusion. On the contrary, our proposed approach advocates for the joint diffusion of rotation and translation. Moreover, our approach applies diffusion on $SE(3)$ within the image space, specifically tailored for the task of object pose estimation.

D Limitations and Broader Impacts

While our score model on $SE(3)$ performs well on the synthetic datasets, there are still limitations in real-world applications. In the SYMSOL experiment, we observed that training a single score model across multiple shapes can be affected by the interactions between the distributions of different objects. This interaction leads to a slight decrease in performance and poses a challenge when extending the model to real-world datasets [65] featuring a wide variety of objects and occlusions.

From an architectural perspective, the current design, which conditions image feature embeddings represented by low-dimensional vector values on the score model, can potentially create a bottleneck due to the limited amount of information it can carry. Therefore, future work could explore better architectures. This might involve integrating high-dimensional image features with the score model or devising improved methods for learning image feature representations. These improvements could allow our score models to be applied in more complex scenarios in the future research endeavors.

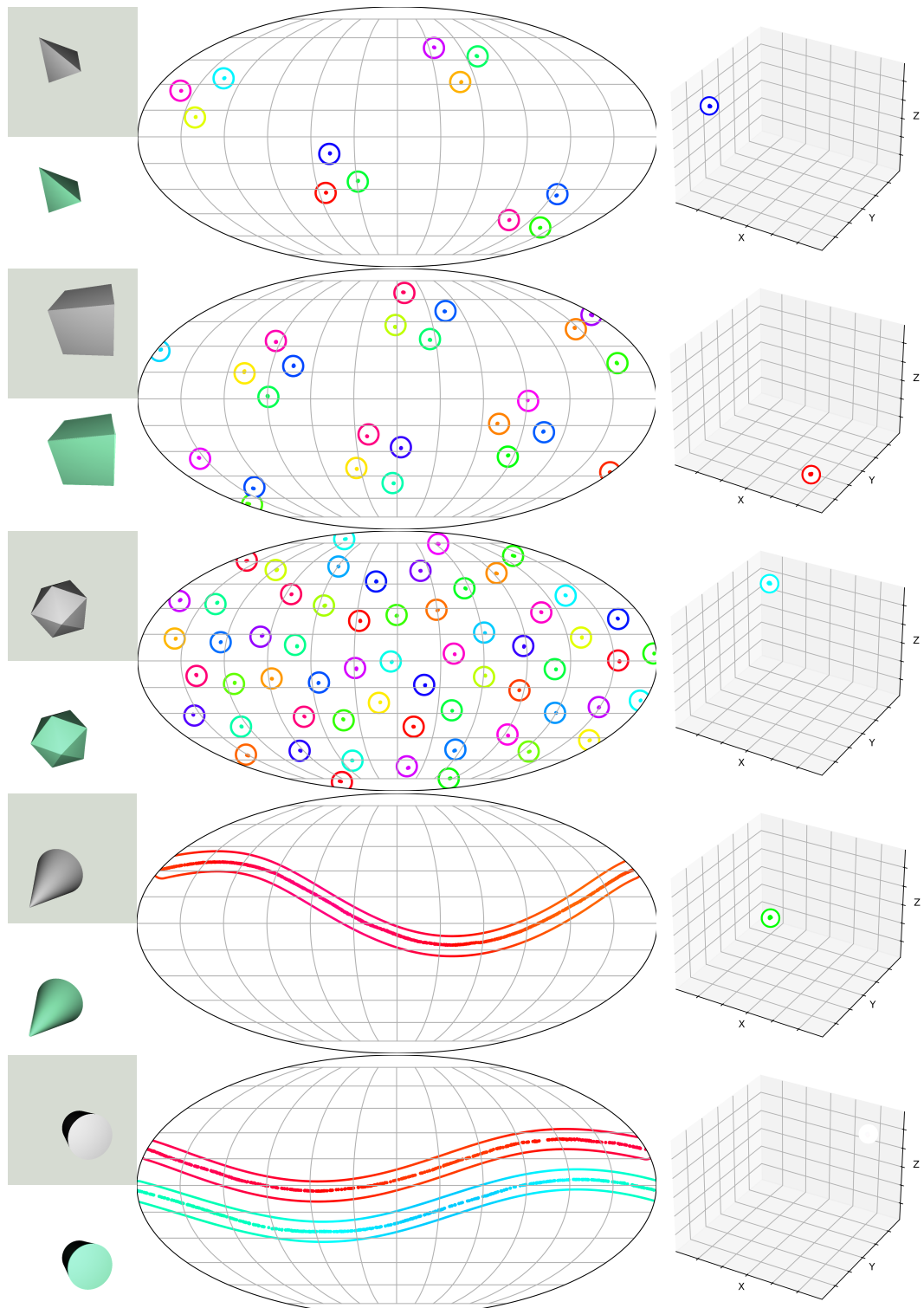


Figure 5: Visualization of our SYMSOL-T results. Please refer to Section A.6 for the detailed descriptions.